Angularly Stable Linear-to-Circular Polarizing Reflectors for Multiple Beam Antennas

Angularly Stable Linear-to-Circular Polarizing Reflectors for Multiple Beam Antennas

Salvador Mercader-Pellicer, Wenxing Tang, Daniele Bresciani, Hervé Legay, *Senior Member, IEEE*
Nelson J. G. Fonseca, *Senior Member, IEEE*, George Goussetis, *Senior Member, IEEE*

***Abstract*— In this paper a new concept to improve the angular stability of linear-to-circular polarizing reflectors is presented. It is first explicitly demonstrated that existing design approaches heavily rely on the adjustment of the design stack-up, namely the substrate height and relative permittivity, to the desired operating frequency. An approach is then proposed for decoupling the performance from the substrate parameters. The proposed approach provides increased design flexibility, resulting in performance improvement. Insight on the operating principle is provided resorting to equivalent circuit models. Subsequently, the benefits of the angularly stable reflection polarizer are demonstrated by a practical example involving a multiple beam antenna implemented using materials and processes compatible with satellite missions. The antenna exploits an innovative quasi-optical beam former as primary feed combined with a cylindrical polarizing reflector. Numerical and experimental results from this antenna architecture are presented to confirm the improvements achieved with the proposed concept over existing designs. The close comparison of simulations with measurements that is achieved validates the concept and the design approach.**

***Index Terms*— linear-to-circular polarizers, frequency selective surfaces, reflector antennas, multiple beam antennas.[1]**

I. Introduction

PERIODIC surfaces providing linear-to-circular (LP-to-CP) polarization conversion have attracted significant interest in the past years due to their advantageous performance characteristics combined with their geometrical simplicity [1]-[7]. They have been considered for applications that include imaging systems [3] as well as satellite communications [4], [5], [6], [8] where they can help to simplify the system optics. For example, the number of components in a millimeter-wave (mm-wave) imaging system can be reduced if the LP-to-CP polarizer and the reflector are combined in the same structure [3]. Similarly, LP-to-CP reflection polarizers provide opportunities to simplify circularly polarized multiple beam antennas (MBAs) such as those used in satellite communication for contiguous coverage in circular polarization [4], [5], [6], [8]. LP-to-CP reflection polarizers also find applications in reflectarrays when LP feeds are preferred [9]. The performance of these structures is traditionally presented under a given plane wave incidence, where the performance is optimized for fixed angles of incidence [1]-[6].

More recently, the performance in the case of illumination from practical feeds and techniques to optimize the polarizing reflector in such scenarios have been presented [7]. These design approaches address the requirements of applications where the reflector is experiencing a fixed illumination. However, in applications such as MBAs the polarizing reflector will typically be illuminated from a number of different feeds (or field patterns), each associated with a different beam [8]. Since the various feeds illuminate the reflector from a distinct angle, optimizing the polarization performance for a given feed will typically lead to compromised performance for others. In this scenario, the angular stability of the polarizing reflector becomes a critical feature.

The bulk of the published literature for this class of reflection polarizers exploits electrically thin substrates [1]-[8]. In this case, the response exhibits overall angularly stable characteristics [1], [2]. While these substrates are suitable for low-cost PCB implementation, their requirements are driven primarily by RF characteristics. In space applications, such as MBAs for satellite communications, substrates need to satisfy simultaneously stringent RF and mechanical characteristics. A reflector assembly considered for reflectarrays that provides both low RF losses and high mechanical stiffness exploits a honeycomb spacer sandwiched between thin laminated skins. Honeycomb spacers are particularly attractive for the manufacturing of shaped reflectors. However, they are not readily available with a thickness below 2 mm, and these electrically thin materials pose challenges for the bonding assembly [10].

In this paper, equivalent circuit models (ECMs) are described in Section II, which provide insight on the operating principle of polarizing reflectors. In particular, these models demonstrate that for electrically thick substrates the operating regime of existing designs may no longer be attainable. This, in turn, is shown to compromise the angular stability as well as operating frequency bandwidth of the polarizing reflector. By exploiting

This paper was submitted on 23 December 2020. This work was supported in part by the European Space Agency under contract 4000107415/12/NL/MH and in part by the European Commission under the REVOLVE project (Grant number: 722840)

S. Mercader-Pellicer was with Heriot-Watt University and is not with Airbus DS, Stevenage, SG1 2AS, United Kingdom.

W. Tang was with Heriot-Watt University and is now with Commscope, Kirkcaldy KY2 6NA, United Kingdom.

D. Bresciani and H. Legay are with Thales Alenia Space, 31100 Toulouse, France (email: {herve.legay}, {daniele.bresciani} @ thalesaleniaspace.com).

N. Fonseca is with the European Space Agency (ESA/ESTEC), Noordwijk, Netherlands (e-mail: nelson.fonseca @ esa.int)..

G. Goussetis is with Heriot-Watt University, Edinburgh, EH14 4AS, United Kingdom (e-mail: g.goussetis @ hw.ac.uk).

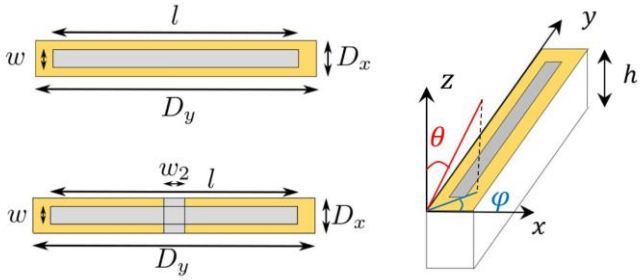

Fig. 1: Layout of unit-cells for reflection polarizers (Left top) the original unconnected dipole element, and (Left bottom) the proposed connected dipole element. The 3D view of the unit-cell for the original unconnected dipole element is shown in (Right).

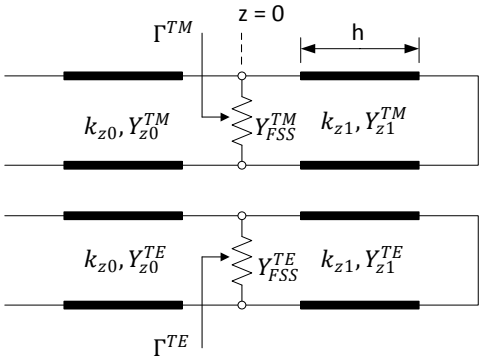

Fig. 2. Equivalent circuit models of a single-layer reflection polarizer for incident TM (top) and TE (bottom) waves.

a previously unused element in the equivalent circuits, we next show that it is possible to decouple the operating principle of the polarizer from the substrate characteristics, and in particular its thickness. Accordingly, the design of a broadband and angularly stable reflection polarizer is demonstrated in the case of a multi-layer honeycomb-based assembly with characteristics driven by mechanical and material constraints. Section III describes a practical example of an antenna architecture exploiting this multi-layer assembly to design a cylindrical reflection polarizer fed by the multiple-beam quasi-optical beamformer (QOBF) presented in [11], [12]. A prototype was manufactured, and the test results are reported and discussed. Finally, some conclusions are drawn in Section IV.

II. Principle of Operation

A. Equivalent Circuit models

A LP-to-CP reflection polarizer works as an anisotropic impedance surface (AIS), which provides polarization conversion by imposing a phase difference of $\pm 90°$ between two orthogonal linear components with equal magnitude and phase [1], [2]. Doubly periodic planar metallo-dielectric dipole arrays, operating as a frequency selective surface (FSS) over a reflective ground plane can be designed to produce the aforementioned phase difference between the two linear incident field components upon reflection [1]-[5]. The high aspect ratio of the periodic element provides the desired anisotropy, Fig. 1. Assuming the incident field is polarized at linear slant 45°, it is a common notation to decompose it into orthogonal linear components, one of which is perpendicular to the dipole array. The transverse electric (TE) wave has its electric field component orthogonal to the incidence plane while the transverse magnetic (TM) wave has its electric field component in the incidence plane. The focus of this paper is on the performance in the *yz*-plane ($\phi = 90°$), as this is a worst case for angular stability due to the larger periodicity. Thus, unless otherwise specified, the notations refer to the *yz*- plane and the TE wave has its electric field component along the x-axis, while the TM wave has its projected electric field component along the y-axis, Fig. 1.

A unit-cell containing the dipole element, often considered in previous works and referred in this paper as the unconnected dipole, is shown in Fig. 1(a). Without loss of generality, the dipole is considered aligned with the *y*-axis. The proposed alternative unit-cell, referred to as the connected dipole, is shown in Fig. 1(b). It consists in a dipole, also aligned with the y-axis, with an added strip along the x-axis, which connects all dipoles along that direction. The rational leading to this unit-cell is elaborated in this section. The same equivalent circuit model can be used for both unit-cells, and is reported in Fig. 2 [2], [5]. In particular, the response of the AIS can be modelled by an equivalent circuit with an admittance representing the FSS in parallel with the short circuit provided by the ground plane at a distance h, where h is the thickness of the dielectric substrate. The response of the AIS is treated independently for TE and TM wave incidence, suggesting that coupling between the two fundamental Floquet modes is negligible. This assumption has been verified in the case of the unconnected dipoles [2], [5], and is also validated here in the case of the proposed connected dipoles.

The transmission lines on the left side of the plane $z = 0$ in Fig. 2 correspond to free-space propagation, with a wavenumber $k_0 = 2\pi/\lambda_0$, and a characteristic admittance $Y_0 = \sqrt{\varepsilon_0/\mu_0}$, where λ_0, ε_0 and μ_0 are the wavelength, the permittivity and the permeability in free-space, respectively. In the dielectric substrate, which is here assumed isotropic for simplicity, the wavenumber is $k_1 = k_0\sqrt{\varepsilon_r}$, while the characteristic admittance is $Y_1 = Y_0\sqrt{\varepsilon_r}$, where ε_r is the relative permittivity of the dielectric material. The wavenumbers along the z-axis under oblique incidence, at an angle θ with respect to the z-axis, are $k_{z0} = k_0\cos\theta$ and $k_{z1} = k_0\sqrt{\varepsilon_r - \sin^2\theta}$ in free-space and in the dielectric material, respectively. It is noted that Snell's law of refraction is employed in order to obtain the latter. The corresponding tangential components of the wavenumbers are $k_{x1} = k_{x0} = k_0\sin\theta$. As shown in Fig. 2, the response of the AIS is driven by its characteristics along the z-axis. The characteristic admittances are $Y_{z0}^{TM} = Y_0/\cos\theta$ and $Y_{z0}^{TE} = Y_0\cos\theta$ for the TM and TE waves in free-space, respectively, while in the dielectric material, they may be written as $Y_{z1}^{TM} = Y_0\varepsilon_r/\sqrt{\varepsilon_r - \sin^2\theta}$ and $Y_{z1}^{TE} = Y_0\sqrt{\varepsilon_r - \sin^2\theta}$ for the TM and TE waves, respectively.

The reflection coefficients $\Gamma^{TM,TE}$, corresponding to the ratio between reflected and incident TM,TE waves respectively, can be expressed as follows

$$\Gamma^{TM,TE} = \frac{Y_{z0}^{TM,TE} - Y_{AIS}^{TM,TE}}{Y_{z0}^{TM,TE} + Y_{AIS}^{TM,TE}} \quad (1)$$

This article has been accepted for publication in a future issue of this journal, but has not been fully edited. Content may change prior to final publication. Citation information: DOI 10.1109/TAP.2020.3048494, IEEE Transactions on Antennas and Propagation

where $Y_{AIS}^{TM,TE}$, the equivalent admittance of the AIS at $z = 0$, is given by

$$Y_{AIS}^{TM,TE} = Y_{FSS}^{TM,TE} - jY_{z1}^{TM,TE}\cot(k_{z1}h) \tag{2}$$

Following an approach similar to the one described in [5], the unit-cells under consideration may be approximated under TM incidence by zero thickness periodic capacitive strips in a dielectric medium of effective permittivity $\varepsilon_{eff} \approx (\varepsilon_r + 1)/2$, since the period along the x-axis is very small compared to the free-space wavelength ($D_x \ll \lambda_0$). For both the unconnected and the connected dipoles, the capacitive strips are defined with a period D_y and an aperture height $D_y - l$. The admittance of the FSS under TM oblique incidence in the *yz*-plane may be analytically approximated by [13, p. 280]

$$Y_{FSS}^{TM} \approx jY_{eff}^{TM}\frac{4D_y\cos\theta}{\lambda_{eff}}\left\{\ln\csc\frac{\pi(D_y-l)}{2D_y} + \frac{1}{2}\frac{(1-\beta^2)^2\left[\left(1-\frac{\beta^2}{4}\right)(A_+ + A_-) + 4\beta^2 A_+A_-\right]}{\left(1-\frac{\beta^2}{4}\right) + \beta^2\left(1+\frac{\beta^2}{2}-\frac{\beta^4}{8}\right)(A_+ + A_-) + 2\beta^6 A_+A_-}\right\} \tag{3}$$

where $A_\pm = \frac{1}{\sqrt{1\pm\frac{2D_y}{\lambda_{eff}}\sin\theta-\left(\frac{D_y\cos\theta}{\lambda_{eff}}\right)^2}} - 1$ and $\beta = \sin\frac{\pi(D_y-l)}{2D_y}$.

The wavelength and characteristic admittance in the equivalent effective dielectric medium are $\lambda_{eff} = \lambda_0/\sqrt{\varepsilon_{eff}}$ and $Y_{eff}^{TM} = Y_0^{TM}\sqrt{\varepsilon_{eff}}$, respectively.

For TE oblique incidence, and as reported in previous works [2], [5], the dipoles are essentially transparent to the electric field component to which they are perpendicular since their width is very small compared to the free-space wavelength ($w \ll \lambda_0$). Thus, the admittance of the FSS may be approximated by zero (open circuit), $Y_{FSS}^{TE} \approx 0$, and the admittance of the AIS is primarily dictated by the substrate thickness and relative permittivity, the angle of incidence and the frequency, leading to $Y_{AIS}^{TE} \approx -jY_{z1}^{TE}\cot(k_{z1}h)$. In previous works [1]-[5], the dielectric slab is selected to match the desired operating frequency range, with an electrical thickness well below $\lambda_0/4$.

Figure 3 illustrates the impact of the main dielectric material parameters, namely the relative permittivity and the substrate thickness, on the phase response using the analytical formulas reported above. These results indicate that for TM incidence, the impact of the substrate is primarily seen near the resonance (defined as the frequency for which the reflection phase is zero degrees). Away from the resonance, the TM phase response is stable over a relatively wide frequency range. For TE incidence, the phase response appears to be more sensitive to the substrate thickness than to the substrate relative permittivity. As reported in Fig. 3(b), the TE reflection characteristics are strongly inductive for thin substrates (e.g. $h = 1.5$ mm) but become capacitive for substrates exceeding $\lambda_0/4$. Full-wave results, obtained with CST Microwave Studio [14], are overlaid in transparency on top of the equivalent circuit model results. These results correspond to the dipole unit-cell (Fig. 1(a)) and

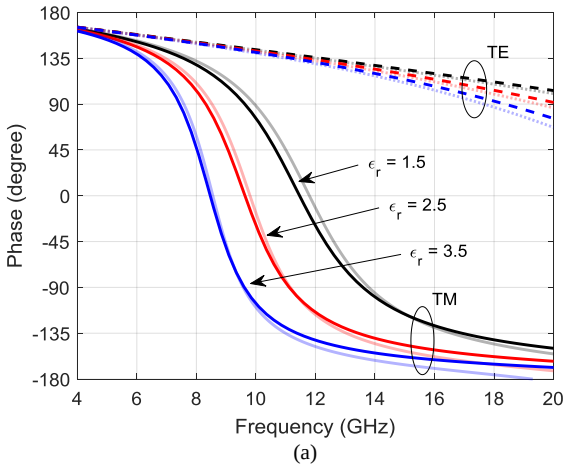

(a)

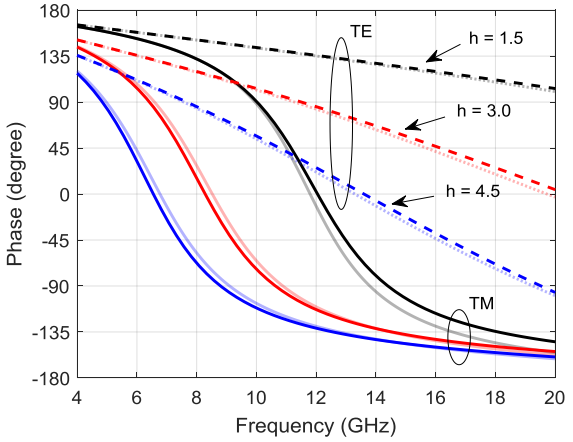

(b)

Fig. 3. Parametric study of the polarizing reflector unit-cell phase response versus dielectric slab properties: (a) relative permittivity for $h = 1.5$ mm and (b) thickness (in mm) for $\varepsilon_r = 1.5$, with $D_y = 8$ mm, $l = 7$ mm, and $D_x \ll D_y$ (CST results are overlaid in transparency on top of ECM results).

validate the capacitive strip approximation. For thinner substrates, the approximation $\varepsilon_{eff} \approx (\varepsilon_r + 1)/2$ provides a reasonably good agreement. For thicker substrates, a slightly smaller value is found to improve the agreement with full-wave results.

From these results, a first key observation is that the operating regime of the polarizer described in previous works is not attainable for electrically thicker substrates. As elaborated in [2], the operating principle of the dipole polarizer relies on a 270° phase difference between the TE and TM reflection phases. This, in turn, can only be achieved if the TE and TM reflection characteristics are inductive and capacitive, respectively, around the design frequency. Fig. 3 indicates that for electrically thick substrates both TE and TM reflection characteristics are capacitive. Consequently, the operation of a polarizer on such a substrate is only achievable with a 90° phase difference between the two field components. Given that the frequency dispersion for the TE component is higher for electrically thick substrates (as shown in Fig. 3(b)), a first conclusion from this equivalent circuit study is that the operation of a dipole polarizer with a thicker substrate is likely to be less stable over frequency.

Next, we investigate the angular stability for the case of

This article has been accepted for publication in a future issue of this journal, but has not been fully edited. Content may change prior to final publication. Citation information: DOI 10.1109/TAP.2020.3048494, IEEE Transactions on Antennas and Propagation

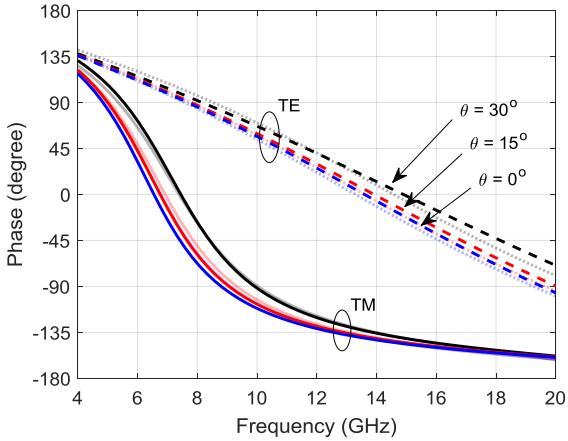

Fig. 4. Parametric study of the polarizing reflector unit-cell phase response versus angle of incidence, with $\varepsilon_r = 1.5$, $h = 4.5$ mm, $D_y = 8$ mm, $l = 7$ mm, and $D_x \ll D_y$ (CST results are overlaid in transparency on top of ECM results).

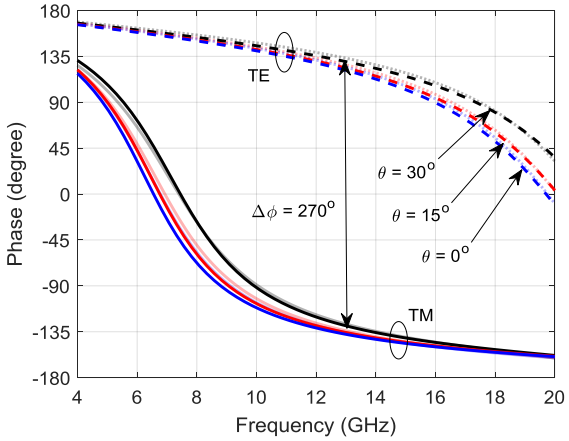

Fig. 5. Parametric study of the connected dipole unit-cell phase response versus angle of incidence, with $\varepsilon_r = 1.5$, $h = 4.5$ mm, $D_y = 8$ mm, $l = 7$ mm, $w_2 = 1$ mm, and $D_x \ll D_y$ (CST results are overlaid in transparency on top of ECM results).

electrically thick substrates. Equivalent circuit model results at oblique incidence are presented in Fig. 4. As shown, the angular variation of the TM component in the region away from the resonance is relatively stable with the angle of incidence. Instead, the reflection of the TE component presents a stronger angular dependence. Accordingly, these results indicate that the angular stability of dipole array reflection polarizers implemented on electrically thicker substrates is compromised when compared to previous reported results [2]. Overlaid CST results also show a good agreement in this case, validating the angular dependence in the equivalent circuit models.

B. Connected Dipoles

Overall, the study above indicates that the favorable characteristics of dipole array polarizers reported in the literature strongly rely on the capacitive admittance of the dipole array for the TM wave in conjunction with the inductive admittance for the TE wave resulting from the electrically thin substrate. Electrically thick substrates shift the TE characteristics towards the capacitive region, with unfavorable impact on the frequency bandwidth and angular stability. Exploiting this observation, it is proposed to replace the open-circuit admittance of the FSS experienced by the TE wave in the *yz*-plane, $Y_{FSS}^{TE} \approx 0$, by an inductive one. In practice, an inductive admittance is achieved with a metallic grid aligned with the tangential component of the electric field, leading the transition from the dipole element to the connected dipole element, Fig. 1. Significantly, and as will also be confirmed below, the introduction of the connecting grid has, to a first approximation, marginal impact on the TM response associated with the unconnected dipole array.

Similarly to the TM incidence, the response of the FSS in the case of the connected dipole may be approximated under TE incidence by zero thickness periodic inductive strips in a dielectric medium of effective permittivity ε_{eff}, with period D_y and metallic width w_2. The admittance of the FSS under TE oblique incidence in the *yz*-plane may be analytically approximated by [13, p. 284]

$$Y_{FSS}^{TE} \approx -jY_{eff}^{TE}/\frac{D_y \cos\theta}{\lambda_{eff}}\left\{\ln \csc\frac{\pi w_2}{2D_y} + \frac{1}{2}\frac{(1-\beta^2)^2\left[\left(1-\frac{\beta^2}{4}\right)(A_+ + A_-) + 4\beta^2 A_+ A_-\right]}{\left(1-\frac{\beta^2}{4}\right) + \beta^2\left(1+\frac{\beta^2}{2}-\frac{\beta^4}{8}\right)(A_+ + A_-) + 2\beta^6 A_+ A_-}\right\} \quad (4)$$

where $A_\pm = \frac{1}{\sqrt{1 \pm \frac{2D_y}{\lambda_{eff}}\sin\theta - \left(\frac{D_y \cos\theta}{\lambda_{eff}}\right)^2}} - 1$ and $\beta = \sin\frac{\pi w_2}{2D_y}$.

This formulation shows an obvious duality with the one reported for the capacitive strips in eq. (3). As shown in Fig. 5, the introduction of the inductive admittance shifts the AIS TE characteristics from the capacitive behavior seen in Fig. 4 to an inductive region. The design parameter w_2 enables to fine tune the admittance Y_{FSS}^{TE}, while the admittance Y_{FSS}^{TM} is primarily driven by the design parameter l for a given period D_y. Thus, to a first approximation, the TE and TM wave resonances may be tuned separately, such that the operating regime becomes similar to the one associated with a thin dielectric substrate. In particular, it is now possible to achieve a polarizing function based on a phase difference of 270° between the two field components and operation in a frequency range away from both TM and TE resonances. This is clearly illustrated in Fig. 5 for a design centered around 13 GHz. The desired phase shift of 270° between the two orthogonal field components is highlighted, with the phase curves showing a good stability both versus frequency and versus the angle of incidence. Overlaid CST results in Fig. 5, obtained with the unit-cell illustrated in Fig. 1(b), confirm that the equivalent model with essentially independent capacitive and inductive responses is valid, to a good degree of approximation.

The description of the operation mode of the proposed polarizing reflector resorting to circuit models with dominant capacitive and inductive contributions provides good physical insight, helping in fine-tuning the various design parameters for a given application. The following section compares the unconnected and connected dipole unit-cells, accounting for real practical implementation constraints.

This article has been accepted for publication in a future issue of this journal, but has not been fully edited. Content may change prior to final publication. Citation information: DOI 10.1109/TAP.2020.3048494, IEEE Transactions on Antennas and Propagation

III. Application to Multiple Beam Antennas

In this section we elaborate on the application of the proposed concept for polarizers in multiple beam antennas, with an emphasis on satellite applications. Section III.A presents design and performance of the polarizer at unit- cell level. Sections III.B and III.C show numerical and experimental results of a practical antenna example, which is compatible with fully space qualified materials and processes and exploits the proposed polarizer.

A. Polarizing Unit-Cell Designs

As highlighted in the introduction, reflector antennas for space applications are commonly manufactured using a honeycomb sandwich structure, with a honeycomb core assembled between two laminate skins, providing favorable mechanical properties. Depending on the desired functionality, RF transparent materials may be integrated in the multi-layer stack-up. The honeycomb sandwich provides the mechanical flexibility required to mold the part. This is particularly of interest to produce curved polarizing reflectors. However, the honeycomb core imposes a minimum thickness. The multi-layer stack-up of the reflector considered in this work is presented in Fig. 6 and comprises a Quartz honeycomb spacer sandwiched between two layers of Astroquartz metalized layers for the ground plane and the FSS printed on the outer sides of the Astroquartz layers. A layer of Pyralux sits on top of the FSS. The thickness of each layer in the stack is shown in Fig. 6, combining Astroquarz ($\epsilon_r = 3.3$, $\tan\delta = 0.01155$), Quartz honeycomb ($\epsilon_r = 1.05$, $\tan\delta = 0.00087$) as spacer and Pyralux ($\epsilon_r = 3.7$, $\tan\delta = 0.037$) as outer layer. The polarizer is designed for operation in Ku-band and optimized at oblique incidence $\theta = 15°$ along the *yz*-plane. In particular, the design target has been an axial ratio (AR) below 1 dB for a frequency band of 10.7-14.5 GHz. With reference to Fig. 1, the unit-cell dimensions are $D_x = 1$ mm and $D_y = 8$ mm, while the dipole dimensions are $l = 5.17$ mm and $w = 0.70$ mm.

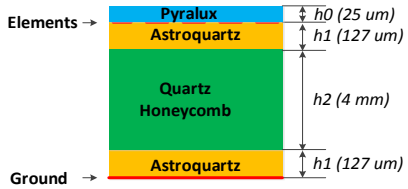

Fig. 6: Cross-section of the polarizing surface comprising a ground plane, two layers of Astroquartz with $\epsilon_r = 3.3$, $\tan\delta = 0.01155$ and 127 µm of thickness, one layer of Quartz honeycomb with $\epsilon_r = 1.05$, $\tan\delta = 0.00087$ and 4 mm of thickness, the printed elements and one layer of Pyralux with $\epsilon_r = 3.7$, $\tan\delta = 0.037$ and 25 µm of thickness.

Fig. 7 presents the reflection phase over frequency for TE and TM wave incidence along the two principal planes for different values of the incidence angle, θ. The simulations were carried out on CST using periodic boundary conditions and plane wave incidence. Following the discussion in Section II, the dipole array was tuned to provide a 90° phase difference between the TE and TM wave incidence. Consequently, both the resonance of the TE and TM waves rest close to the operating frequency. As expected, the phase response is

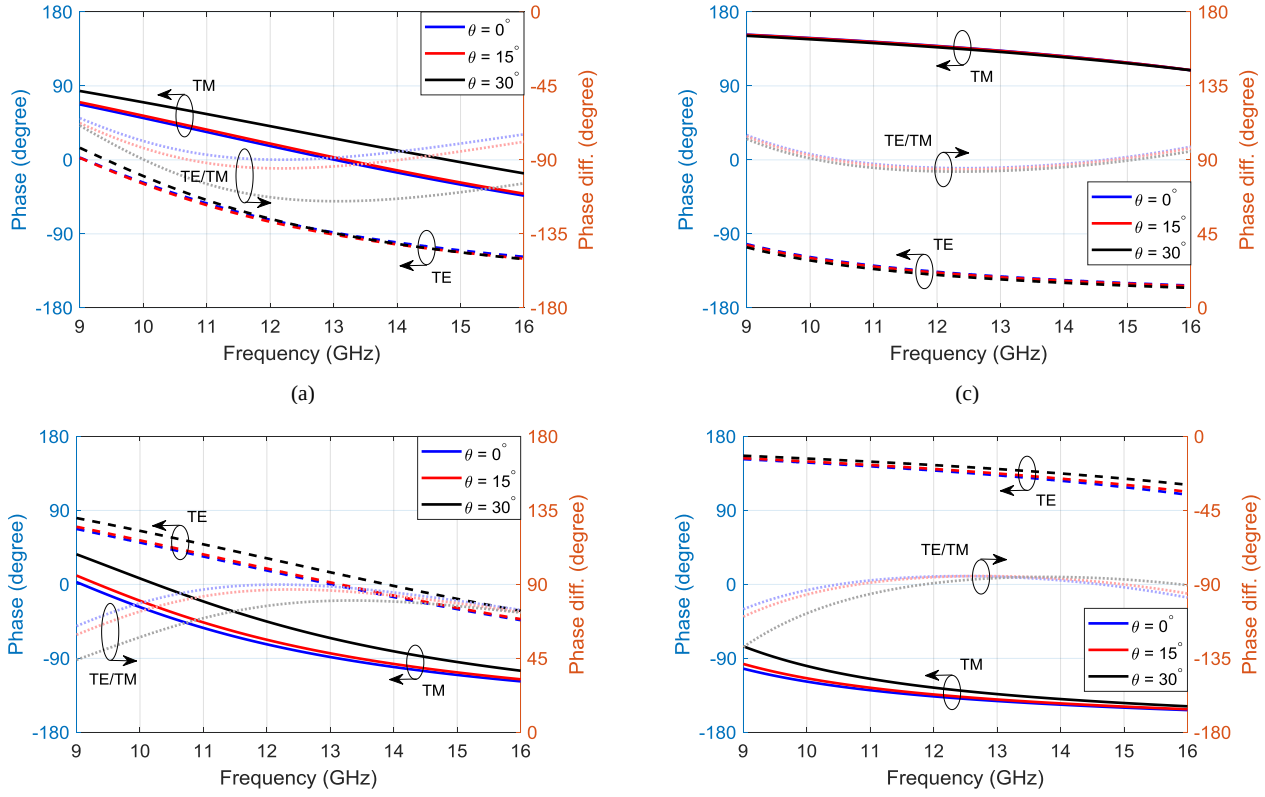

Fig. 7: Absolute and differential values of the polarizing reflector unit-cell phase response versus angle of incidence obtained with CST for the unconnected dipole (a) in the *xz*-plane ($\phi = 0°$) and (b) in the *yz*-plane ($\phi = 90°$), and for the connected dipole (c) in the *xz*-plane ($\phi = 0°$) and (d) in the *yz*-plane ($\phi = 90°$).

This article has been accepted for publication in a future issue of this journal, but has not been fully edited. Content may change prior to final publication. Citation information: DOI 10.1109/TAP.2020.3048494, IEEE Transactions on Antennas and Propagation

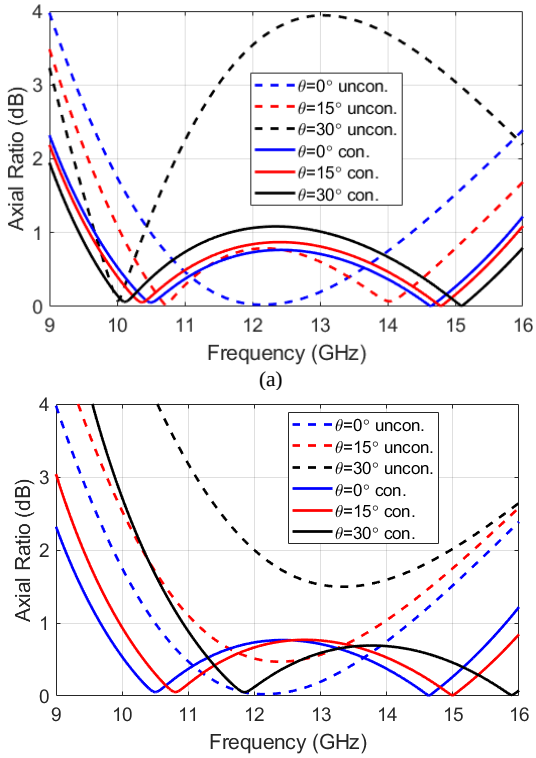

Fig. 8: Axial ratio of the unconnected (dashed lines) and connected (solid lines) dipoles under plane wave incidence at different angles in the two principal planes: (a) *xz*-plane ($\phi = 0°$) and (b) *yz*-plane ($\phi = 90°$).

sensitive to the incidence angle and significant variations are visible already for $\theta = 30°$. In the *xz*-plane, the impact of the thick substrate is clearly visible for the TM wave, which has an electric field component perpendicular to the dipoles in that plane, while the impact of the substrate on the TE wave is marginal. This is in line with expectations as the response to the TM wave is primarily defined by the substrate characteristics, while the response to the TE wave is dependent on the FSS and its projection, seen as capacitive strips, remains fairly the same

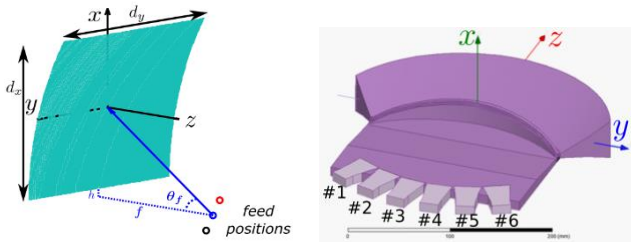

Fig. 9: Cylindrical offset reflector antenna with radius 1 m, projected aperture with dimensions $d_x = 0.5$ m, $d_y = 0.6$ m, distance between reflector and feed $f = 0.48$ m, clearance $h = 0.025$ m and offset angle $\theta_f = 30°$.

at oblique incidence in that plane. In the *yz*-plane, both field components are affected, which improves the phase difference to some extent. The effect on the TM wave, which has an electric field component aligned with the dipoles, is more significant, as the geometry of the projected capacitive strips varies with the angle of incidence in that plane. These results are expressed in terms of axial ratio in Fig. 8, with dashed lines corresponding to the unconnected dipole. It confirms the sensitivity of the design to incidence angle, with a worst case of about 4 dB within the operating frequency bandwidth at $\theta = 30°$ in the *xz*-plane.

Using the same stack, a connected dipole array is also designed (Fig. 1(b)). For comparison purposes, the unit-cell dimensions are unchanged, $D_x = 1$ mm and $D_y = 8$ mm. The remaining dimensions are optimized for the requirements leading to $l = 6.94$ mm, $w = 0.65$ mm, and $w_2 = 1$ mm. As detailed in Section II.A, the modified unit-cell is tuned to provide a 270° phase difference between TE and TM incidence. The reflection phase results obtained with CST are also reported in Fig. 7. The improvement is clearly visible, particularly in the *xz*-plane. In the *yz*-plane, there is a slight variation for TM wave incidence, with the electric field component along the dipoles. This is because of the resonance of the capacitive strips, which would require to increase the period D_y so as to bring the resonance further down and increase both the frequency and angular stability. However, this parameter is constrained by the

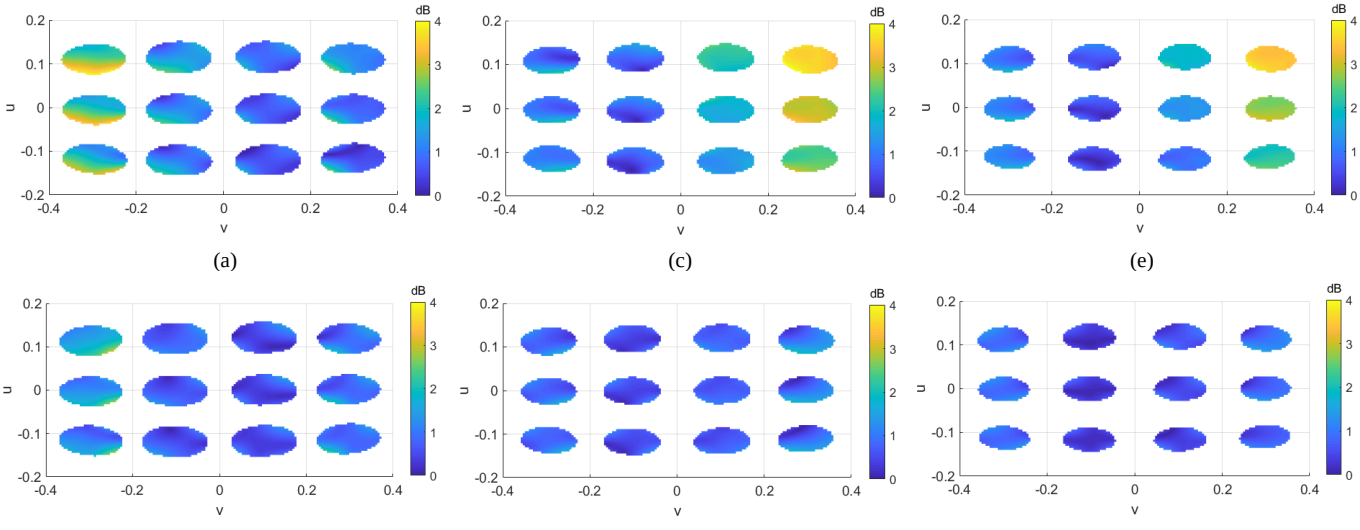

Fig. 10: Far-field axial ratio within the 4 dB beamwidth for the polarizing surface with unconnected and connected dipoles at (a), (b) 10.7 GHz; (c), (d) 12.6 GHz; (e), (f) 14.5 GHz, with (a), (c), (e) corresponding to the original unconnected dipoles design while (b), (d), (f) refer to the proposed connected dipoles design.

This article has been accepted for publication in a future issue of this journal, but has not been fully edited. Content may change prior to final publication. Citation information: DOI 10.1109/TAP.2020.3048494, IEEE Transactions on Antennas and Propagation

TABLE I
RMS VALUES OF AXIAL RATIO FOR EACH FAR-FIELD BEAM IN FIG. 10

	10.7 GHz		12.6 GHz		14.5 GHz	
Beam	uncon.	conn.	uncon.	con.	uncon.	con.
$\boldsymbol{u} = \mathbf{0}$, #2	1.08	1.02	3.01	1.07	2.76	0.85
$\boldsymbol{u} = \mathbf{0}$, #3	0.78	0.62	1.71	0.77	1.35	0.57
$\boldsymbol{u} = \mathbf{0}$, #4	1.33	0.75	0.83	0.60	0.58	0.38
$\boldsymbol{u} = \mathbf{0}$, #5	2.41	1.47	1.14	0.91	1.18	0.95
$\boldsymbol{u} = -\mathbf{0.12}$, #2	0.88	1.06	2.49	0.99	2.18	0.71
$\boldsymbol{u} = -\mathbf{0.12}$, #3	0.70	0.62	1.40	0.73	0.96	0.51
$\boldsymbol{u} = -\mathbf{0.12}$, #4	1.19	0.70	0.75	0.62	0.49	0.40
$\boldsymbol{u} = -\mathbf{0.12}$, #5	2.09	1.27	1.24	0.92	1.20	0.91
$\boldsymbol{u} = \mathbf{0.12}$, #2	1.39	1.01	3.61	1.18	3.47	1.00
$\boldsymbol{u} = \mathbf{0.12}$, #3	0.97	0.63	2.16	0.83	1.86	0.67
$\boldsymbol{u} = \mathbf{0.12}$, #4	1.53	0.85	0.95	0.55	0.76	0.35
$\boldsymbol{u} = \mathbf{0.12}$, #5	2.77	1.74	1.09	0.90	1.08	0.95

Beam numbering is with reference to the $\boldsymbol{u}$ coordinate and Fig. 9(b)

appearance of higher order Floquet modes (i.e. grating lobes). The axial ratio of the connected dipole is reported in solid lines in Fig. 8, and remains mostly below 1 dB over the considered frequency range and angular range.

B. Antenna Configuration and Simulated Performance

A curved reflector fed by a line source is considered here [16], [17]. The reflector geometry is described in Fig. 9(a). The feed system is the QOBF described in [11], [12], reported in Fig. 9(b), and has 6 beam ports. The dimensions of the QOBF and pointing angles associated with each port are detailed in [12]. As the QOBF already provides focused beams in the *yz*-plane with reference to the coordinate system in Fig. 9, the reflector geometry has to operate as a planar mirror in that plane (i.e. no magnification effect), while focusing the field in the orthogonal plane. A cylindrical reflector is considered here for this purpose. Although the selected circular profile in the offset

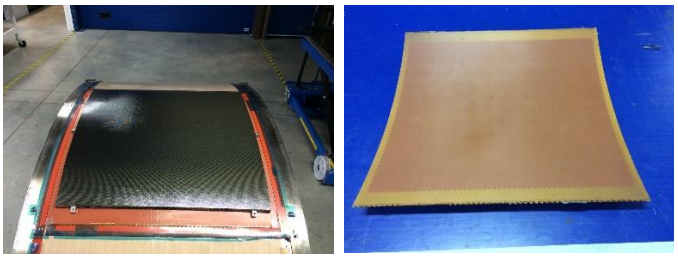

(a) (b)

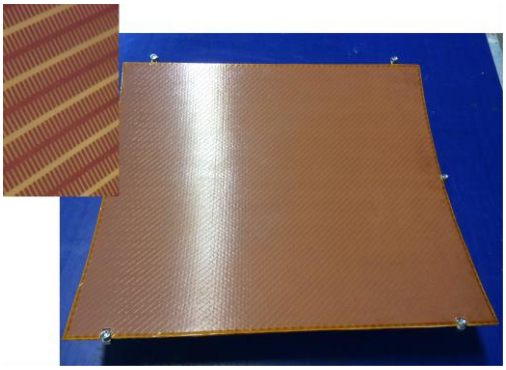

(c)

Fig. 11: Different steps of the manufacturing process: (a) backing structure, (b) polarizing surface and (c) final polarizing reflector.

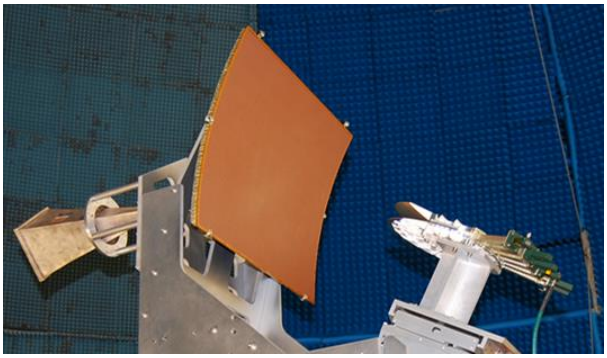

Fig. 12: Multiple beam antenna under test, combining the proposed connected dipole cylindrical polarizing reflector and a QOBF.

plane introduces aberrations (no focal point), it provides more stable scanning performance over a wider angular range when compared to a parabolic profile. The dimensions of the reflector are $d_x = 500$ mm and $d_y = 600$ mm. The distance between the reflector and feed (blue circle in Fig. 9(a)), the reflector clearance, the radius of the cylinder and the offset are $f = 480$ mm, $h = 25$ mm, $R = 1$ m and $\theta_f = 30°$, respectively.

For this antenna geometry, the incidence angle experienced at the center of the reflector as seen from the feed position is $\theta = 15°$ (Fig. 9(a)). The two designs presented in Section II.B have been optimized for this incidence angle, in connection with this antenna architecture, to provide good polarization conversion within the angular range corresponding to the field of view of the reflector. We proceed to computing the far-field characteristics of the reflector antenna considering the different incidences from the different output ports of the QOBF and assuming the polarizer unit-cell is laid on the reflector. Since the QOBF is vertically polarized (along the x-axis in Fig. 9(b)), the unit-cells have to be laid at slant 45°.

The far-field of the polarizing reflector is computed as follows. First, a spherical wave expansion (SWE) [18] is used to obtain the approximate near-field incident on the reflector surface from the far-field of the QOBF. The Poynting vector is used to compute the angle of incidence at each unit-cell. Then a database of S-parameters produced by the unit-cell under full periodic conditions and plane wave incidence for each angle of incidence is created using CST. Since these S-parameters and the angles of incidence refer to the fundamental modes of the Floquet expansion (i.e. no grating lobes), the fundamental modes are extracted from the total incident field [7]. Then they are combined with the S-parameters to obtain the reflected field at each unit-cell. The reflected field is used to obtain the equivalent surface currents, and the latter are integrated over the reflector surface to obtain the far-field [19], [20]. The in-house modelling tool has earlier been used in [7] demonstrating good agreement with experimental results.

With reference to Fig. 9(b), next we study the performance assuming excitation of ports #2 to #5 of the QOBF. In order to check the multiple beam capabilities also in the vertical plane, two more QOBFs are simulated on top and at the bottom of the central one, as shown by the red and black circles in Fig. 9(a), corresponding to an antenna architecture fed by a stack of QOBFs. Fig. 10 shows the far-field axial ratio within the 4 dB beamwidth across the operating frequency range, at 10.7 GHz,

This article has been accepted for publication in a future issue of this journal, but has not been fully edited. Content may change prior to final publication. Citation information: DOI 10.1109/TAP.2020.3048494, IEEE Transactions on Antennas and Propagation

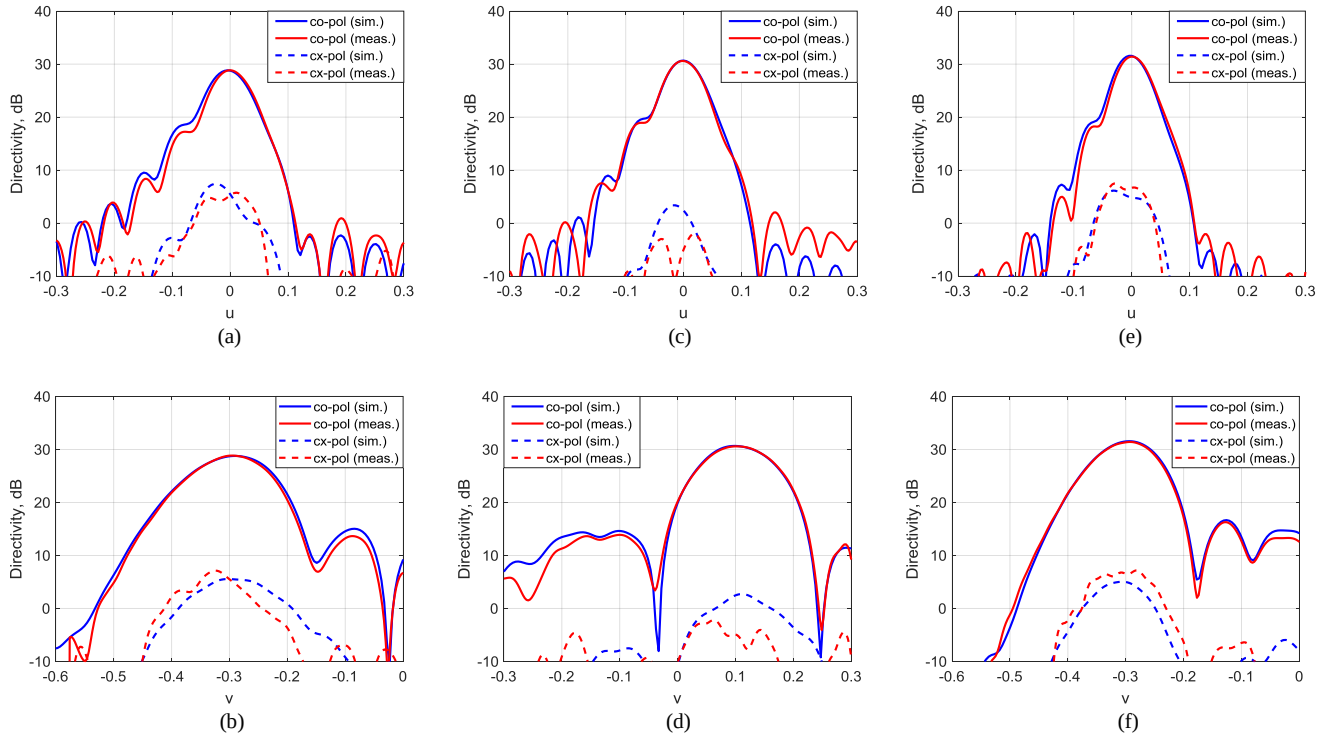

Fig. 13: Comparison of simulated and measured directivity patterns for the QOBF fed cylindrical reflector (a), (b) at 10.7 GHz for port #2; (c), (d) at 12.6 GHz for port #4; (e), (f) at 14.5 GHz for port #2, with (a), (c), (e) corresponding to cuts in the vertical plane ($v = 0$), while (b), (d), (f) refer to the horizontal plane ($u = 0$).

12.6 GHz and 14.5 GHz. Due to the angular variation of the axial ratio response associated with the unconnected dipoles (Fig. 8), the associated far-field axial ratio deteriorates (up to 4 dB) for beams far from the center. A significant improvement is observed when the connected dipole design is used. In order to quantify this improvement, Table I shows the root mean square (RMS) values for the axial ratio in every beam at three frequencies and for both designs. The feed numbering in Table I refers to Fig. 9(b). As reported in Table I, the improvement of the axial ratio RMS by virtue of the connected dipole is up to 1.02 dB at 10.7 GHz. Similarly, the axial ratio RMS improvement is up to 2.43 dB and 2.45 dB at 12.6 GHz and 14.5 GHz, respectively.

C. *Manufacturing and Measurements*

In order to validate the results of the connected version, a polarizing reflector with the connecting line using the geometry of Fig. 9 was manufactured and tested. The manufacturing process is divided in three steps. The first step involves the manufacturing of the backing structure on a cylindrical reflector consisting of a composite panel of Quartz honeycomb that spaces apart rear and front Astroquartz skins, as seen in Fig. 11(a). The second step involves the manufacturing of the polarizing surface on a single mold consisting on the Quartz honeycomb core with two plies of Astroquartz on each side, the elements, printed with their nominal dimensions on a flat surface, and the Pylarux ply as seen in Fig. 11(b). Finally, the last step involves the assembly of the polarizing surface and the backing structure as seen in Fig. 11(c). Fig. 11(c) also includes a zoom on the polarizing reflector where it is possible to see the dipoles at slant 45° and the connecting line.

The measurements of the polarizing surface with the connected dipole were carried out at the outdoor test range of Thales Alenia Space facilities in Toulouse. The complete antenna under test, comprising the polarizing reflector and the QOBF, is shown in Fig. 12. A selective comparison of the simulated and measured patterns along the two principle planes can be found in Fig. 13. It is noted that numerical simulations have confirmed that the polarizer does not noticeably affect the co-polarization patterns when compared with a fully metallized reflector. The QOBF was placed at the original position (blue circle in Fig. 9(a)). The ports used in this comparison are ports #2 at 10.6 GHz, #4 at 12.6 GHz and #2 at 14.5 GHz. Even though there are some minor differences, attributed to manufacturing and modelling imperfections, overall a very good agreement in both co- and cross-polarization components is observed. This serves as validation of the proposed solution the analysis method.

IV. Conclusion

In this paper, we propose a concept to improve the angular stability of reflection polarizers based on doubly periodic metallo-dielectric arrays printed on grounded dielectric substrate. The concept exploits a wire grid geometry on the polarizer, which reduces the dependence of the reflection characteristics on the substrate for a linearly polarized incident field aligned in the same plane. Consequently, the associated dependence on the incidence angle is reduced and the angular stability of the polarizing surface can be improved. The benefits of the proposed design are relevant to multiple beam antennas, such as those deployed in satellite communication systems. This has been demonstrated by means of an innovative multiple beam antenna architecture. A test campaign on a manufactured

prototype reveals very good agreement between simulations and measurements, thereby providing experimental validation.

V. Acknowledgment

The authors would like to thank Mr. Daniel Calas for manufacturing the prototype and the anonymous reviewers and the Editorial Board for valuable comments that helped significantly improve the quality of this work.

References

[1] K. Karkkainen and M. Stuchly, "Frequency selective surface as a polarisation transformer," in *IEEE Proc. Microw., Anten. Propag.*, vol. 149, no. 56, pp. 248-252, Oct. 2002.

[2] E. Doumanis, G. Goussetis, J.L. Gómez-Tornero, R. Cahill, and V. Fusco, "Anisotropic impedance surfaces for linear to circular polarization conversion," in *IEEE Trans. Anten. Prop.*, vol. 60, no. 1, pp. 212-219, Jan 2012.

[3] E. Doumanis, G. Goussetis, R. Dickie, R. Cahill, P. Baine, M. Bain, V. Fusco, J.A. Encinar, G. Toso, "Electronically reconfigurable liquid crystal based mm-wave polarization converter," *IEEE Trans. Antennas Propag.*, Vol. 62, No. 4, pp. 2302-2307, 2014

[4] N.J.G. Fonseca and C. Mangenot, "Low-profile polarizing surface with dual-band operation in orthogonal polarizations for broadband satellite applications," in *Proc. 8th Eur. Conf. Antennas Propag. (EuCAP'14)*, The Hague, Netherlands, 2014.

[5] N.J.G. Fonseca and C. Mangenot, "High-performance electrically thin dual-band polarizing reflective surface for broadband satellite applications," in *IEEE Trans. Antennas Propag.*, vol. 64, no. 2, pp. 640-649, Feb 2016.

[6] W. Tang, S. Mercader-Pellicer, G. Goussetis, H. Legay and N.J.G. Fonseca, "Low-profile compact dual-band unit cell for polarising surfaces operating in orthogonal polarizations," in *IEEE Trans. Antennas Propag. Comm.*, vol. 65, no. 3, pp. 1472-1477, March 2017.

[7] S. Mercader-Pellicer, G. Goussetis, G.M. Medero, H. Legay, D. Bresciani, N.J.G. Fonseca "Cross-Polarization Reduction of Linear-to-Circular Polarizing Reflective Surfaces," *IEEE Antennas and Wireless Propagation Letters*, vol. 18, no. 7, pp. 1527-1531, July 2019

[8] S. Mercader-Pellicer, G. Goussetis, G.M. Medero, H. Legay, D. Bresciani, N.J.G. Fonseca, "Dual Ka-band multiple beam reflector antenna for Western European coverage," in *Proc. 13th Eur. Conf. Antennas Propag. (EuCAP'19)*, Krakow, Poland, 2019.

[9] G.B. Wu, S.W. Qu, S. Yang and C.H. Chan, "Broadband, single-layer dual circularly polarized reflectarrays with linearly polarized feed," *IEEE Trans. Antennas Propag.*, vol. 64, no. 10, pp. 4235–4241, Oct. 2016.

[10] M. Zhou, M.F. Palvig, S. B. Sørensen, J. Rosenkrantz de Lasson, D. Marote Alvarez, M. Notter, D. Schobert, "Design of Ka-band Reflectarray Antennas for High Resolution SAR Instrument," 14th European Conference on Antennas and Propagation (EuCAP), 15-20 March 2020.

[11] F. Doucet, N.J.G. Fonseca, E. Girard. H. Legay, R. Sauleau, "Analytical Model and Study of Continuous Parallel Plate Waveguide Lens-like Multiple-Beam Antennas," *IEEE Trans. Antennas Propag.*, Vol. 66, No. 9, pp. 4426-4436, 2018

[12] F. Doucet, N.J.G. Fonseca, E. Girard, X. Morvan, L. Le Coq, H. Legay, R. Sauleau, "Shaped Continuous Parallel Plate Delay Lens With Enhanced Scanning Performance," *IEEE Trans.Antennas Propag.*, Vol. 67, No. 11, pp. 6695-6704, 2019.

[13] N. Marcuvitz, "Waveguide Handbook: Chapter 5 – Four-terminal structures," McGraw-Hill Book Company, Inc., 1951.

[14] CST Studio Suite. [Online]: https://www.cst.com/products/ 303 csts2.

[15] G. Goussetis, A.P. Feresidis, J.C. Vardaxoglou, "Tailoring the AMC and EBG Characteristics of Periodic Metallic Arrays Printed on Grounded on Grounded Dielectric Substrate," *IEEE Trans, Antennas Propag.*, Vol. 54, No. 1, pp. 82-89, January 2006

[16] N.J.G. Fonseca, E. Girard, H. Legay, "Hybrid array fed reflector antenna solution for broadband satellite communications," 11th European Conference on Antennas and Propagation (EUCAP), 2017.

[17] N.J.G. Fonseca, E. Girard, H. Legay, "Doubly curved reflector design for hybrid array fed reflector antennas," IEEE Trans. Antennas Propag., vol. 66, no. 4, pp. 2079-2083, Apr. 2018.

[18] J.E. Hansen, *Spherical Near-Field Antenna Measurements*, Peter Peregrinus Ltd., London, 1988.

[19] C. Balanis, "Chapter 12 – Aperture antennas," in *Antenna Theory: Analysis and Design*, 3rd Ed., Wiley & Sons, pp. 653-738.

[20] S.K. Sharma, S. Rao and L. Shafai, "Chapter 2 – Numerical techniques for reflectors," in *Handbook of Reflector Antennas and Feed Systems*, Artech House, 2013, pp. 13-65.

[21] W. Tang, G. Goussetis, N.J.G. Fonseca, H. Legay, E. Sáenz, P. de Maagt, "Coupled split-ring resonator circular polarization selective surface," *IEEE Trans. Antennas Propag.*, Vol. 65, No. 9, pp. 4664-4675, 2017.

Salvador Mercader-Pellicer was born in Murcia, Spain, in 1988. He received the B.Eng. degree in telecommunications engineering (with a specialization in telematics) and M.Sc. degree in telecommunications engineering from the Universidad Politecnica de Cartagena (UPCT), Cartagena, Spain, in 2010 and 2013, respectively, and the PhD degree from Heriot-Watt University, Edinburgh, U.K. in 2018.

He works in the Antenna Group of Airbus Defence & Space, based on Stevenage, U.K. His research interests include the analysis and design of reflector antennas, phased arrays, frequency-selective surfaces, and reflect-arrays with application on multiple beam antennas for satellite communication systems.

Wenxing Tang (S'08–M'15) received M.Sc. (distinction) and Ph.D. degrees in Institute of Sensors, Signals and Systems at Heriot-Watt University, Edinburgh, U.K., in 2005 and 2011, respectively. From 2011 and 2018, he was a Postdoctoral Research Associate at the Microwave and Antenna Engineering Research Group, Heriot-Watt University, holding a good publication record of peer-reviewed papers and patent. He currently joins Commscope U.K. as an RF Engineer, mainly responsible for the research and development of phased array, W/D band antenna, reflector antenna, reflector arrays and passive components.

Daniele Bresciani was born on February the 27th, 1958. He graduated in 1982 at Politecnico di Torino, Italy. His fields of Interest are study, analysis and design of reflector antenna systems with particular emphasis on Reflect-arrays and Frequency or Polarization Selective Surfaces (FSS or Dichroics), for applications such as satellite communications (radio links, terrestrial coverages, etc); development of theoretical models and computer codes aimed to electromagnetic design and graphic applications. His major skills are reflect-arrays and FSS study and design, complex reflector systems analysis, dielectric and dichroic lenses synthesis and analysis, near field fast reconstruction. His present job is at ThalesAleniaSpace France in Toulouse at Research Department, carrying on studies and codes development on reflect-array subject (electrical design and measurements).

Hervé Legay received the electrical engineering and Ph.D. degrees from the National Institute of Applied Sciences, Rennes, France, in 1988 and 1991, respectively. He was then a Post-Doctoral Fellow with the University of Manitoba, Winnipeg, MB, Canada.

In 1994, he joined Alcatel Space (now Thales Alenia Space), Toulouse, France. He initially conducted studies in the areas of military telecommunication satellite antennas and antenna processing. He designed the architecture and the antijamming process of the Syracuse 3 active antenna. He is currently the Head of the R&T on space antennas, developing new antenna concepts with emerging technologies (Reflectarrays, integrated antennas, multiple beam quasi-optical antennas, innovative active architectures, antenna processing,…). He is co-Director of the joint laboratory MERLIN, involving Thales Alenia Space, and the Institut d'Electronique et de Télécommunication de Rennes. Dr. Legay is the Chair of a group of Antenna Experts in Thales Group. He coordinates the collaborations with academic and research partners. He has authored 35 patents. He was a co-prize winner of the 2007 Schelkunoff Prize Paper Award. He was a recipient of

the Gold Thales Awards in 2008, a reward for the best innovations in the Thales Group.

Nelson J. G. Fonseca (M'06, SM'09) was born in Ovar, Portugal, in 1979. He received the M.Eng. degree from Ecole Nationale Supérieure d'Electrotechnique, Electronique, Informatique, Hydraulique et Télécommunications (ENSEEIHT), Toulouse, France, in 2003, the M.Sc. degree from the Ecole Polytechnique de Montreal, Quebec, Canada, also in 2003, and the PhD degree from Institut National Polytechnique de Toulouse – Université de Toulouse, France, in 2010, all in electrical engineering.

He works in the Antenna and Sub-Millimetre Waves Section, European Space Agency (ESA), Noordwijk, The Netherlands. His current research interests include multiple beam antennas for space missions, beam-former theory and design, ground terminal antennas and novel manufacturing techniques. He has authored or co-authored more than 210 papers in peer-reviewed journals and conferences. He contributed to 25 technical innovations, protected by over 40 patents issued or pending.

Dr. Fonseca served as the Chair of the 38th ESA Antenna workshop on Innovative Antenna Systems and Technologies for Future Space Missions, October 2017, and as the Co-Chair of the 2018 IET Loughborough Antennas & Propagation conference (LAPC 2018). He is currently serving as an Associate Editor for the *IET Microwave, Antennas and Propagation (MAP) journal* and for the *IEEE Transactions on Microwave Theory and Techniques (TMTT)*, and as a Topic Editor for the *IEEE Journal of Microwaves (JMW)*. He is also serving as Vice Chair of the newly founded *Technical Committee 29 (TC-29)* on Microwave Aerospace Systems of the *IEEE MTT Society*. He is a board member of the European School of Antennas (ESoA) since January 2019 and the elected EurAAP Regional Delegate representing Benelux for the term 2021-2023. He received several prizes and awards, including the Best Young Engineer Paper Award at the 29th ESA Workshop on Antennas in 2007 as well as multiple ESA Technical Improvement Awards.

George Goussetis (S 99, M 02, SM 12) received the Diploma degree in Electrical and Computer Engineering from the National Technical University of Athens, Greece, in 1998, and the Ph.D. degree from the University of Westminster, London, UK, in 2002. In 2002 he also graduated B.Sc. in physics (first class) from University College London (UCL), UK.

In 1998, he joined the Space Engineering, Rome, Italy, as RF Engineer and in 1999 the Wireless Communications Research Group, University of Westminster, UK, as a Research Assistant. Between 2002 and 2006 he was a Senior Research Fellow at Loughborough University, UK. He was Assistant Professor with Heriot-Watt University, Edinburgh, UK between 2006 and 2009 and Associate Professor with Queen's University Belfast, UK, between 2009 and 2013. In 2013 he joined Heriot-Watt and was promoted to Professor in 2014. He currently directs the Institute of Sensors Signals and Systems at Heriot-Watt University. He has authored or co-authored over 500 peer-reviewed papers five book chapters one book and four patents. His research interests are in the area of microwave and antenna components and subsystems.

Dr. Goussetis held research fellowships from the Onassis foundation in 2001, the UK Royal Academy of Engineering between 2006-2011, and European Commission Marie-Curie in 2011-12 and again in 2014-17. He is the co-recipient of the 2011 European Space Agency young engineer of the year prize, the 2011 EuCAP best student paper prize, the 2012 EuCAP best antenna theory paper prize and the 2016 Bell Labs prize. He served as Associate Editor to the IEEE Antennas and Wireless Propagation Letters between 2014-18.